Beyond plasmonic enhancement of the transverse magneto-optical Kerr effect with low-loss high-refractive-index nanostructures

William O. F. Carvalho [1,*] E. Moncada-Villa,[2] Osvaldo N. Oliveira, Jr.,[3] and J. R. Mejía-Salazar [1,†]

[1]*National Institute of Telecommunications (Inatel), Santa Rita do Sapucaí, MG 37540-000, Brazil*

[2]*Escuela de Física, Universidad Pedagógica y Tecnológica de Colombia, Avenida Central del Norte 39-115, Tunja, Colombia*

[3]*Instituto de Física de São Carlos, Universidade de São Paulo, CP 369, 13560-970, São Carlos, SP, Brazil*

(Received 28 September 2020; revised 12 December 2020; accepted 1 February 2021; published 9 February 2021)

We demonstrate a concept for a large enhancement of the transverse magneto-optical Kerr effect (TMOKE) in the transmission mode. The concept exploits diffracted waves from dielectric-MO grating ribs to excite the guided modes in a high-refractive-index planar waveguide, thus opening different routes for efficient, integrated, and low-loss magneto-optical devices. The high Q factors from very narrow peaks may permit applications in high-resolution sensing/biosensing.

DOI: 10.1103/PhysRevB.103.075412

I. INTRODUCTION

The modulation of near- and far-field optical properties with magneto-optical effects is promising for applications such as filters, sensors, modulators, routers, data storage, and spintronic devices [1–9]. For example, biosensing and magnetization monitoring [10–14] have been exploited through enhancing the transverse magneto-optical (MO) Kerr effect (TMOKE), i.e., the relative change in the intensity of transmitted or reflected light when the transversal magnetization is flipped. These applications are based on strongly enhanced electromagnetic fields in magnetoplasmonic platforms [15–17], because TMOKE in conventional ferromagnetic materials is usually not large enough for practical purposes. Unfortunately, in spite of the large TMOKE enhancements in reflection [2] and transmission [18] modes, the magnetoplasmonic approach is limited due to the strong absorption associated with Ohmic losses from metal inclusions, mainly at optical and infrared wavelengths. This last drawback has motivated the use of low-loss high-refractive-index (HRI) nanostructures for light enhancement and confinement [19–21]. Indeed, dielectric Si nanodisks placed on a ferromagnetic film have been used for enhancing the Faraday magneto-optical effect [20], and one-dimensional dielectric gratings yielded enhanced TMOKE amplitudes in the reflection mode, but not in the transmission mode (low amplitudes of the order of 10^{-3}) [19,21,22]. One possible strategy to address the latter limitation is to explore the resonant coupled modes using dielectric gratings [23–25]. In particular, the ability to couple diffracted waves in dielectric gratings with guided modes into a HRI film placed below the grating can be used to resemble the main plasmonic feature, i.e., to produce deep reflection/transmission peaks. These modes can be considered the dielectric counterpart of the waveguide-plasmon-polariton approach [18,26,27].

In contrast to previous dielectric grating designs [21,22], which produced experimental TMOKE amplitudes in transmission up to ca. 1%, we introduce a design with a grating of dielectric-MO ribs on an AlSb HRI slab surrounded by air and grown on a SiO_2 substrate, as schematized in Fig. 1. The grating ribs are made of cerium-substituted yttrium iron garnet (Ce:YIG) material, which can be combined with III-V or Si-based semiconductors [28–31]. Experimental methods such as physical vapor deposition [29] or pulsed laser deposition [30] may be used to fabricate these multilayer systems. The strongly enhanced and localized electromagnetic fields inside the guiding slab become distributed inside the adjacent ribs, thus improving their MO activity. The magnetization sense along the rib axes was used to control the resonant angle/wavelength of the grating and thus the corresponding coupling to the waveguide modes. Significantly, our system exhibits similar or even higher TMOKE amplitudes than its plasmonic counterpart. While TMOKE amplitudes around 10% were reported for the waveguide-plasmon polariton mechanism [18,32], here we show amplitudes up to 15% using a low-loss HRI nanostructure.

II. THEORETICAL FRAMEWORK

Figure 1 shows the structure designed to yield an enhanced TMOKE, which is a measure of the relative change in the transmission amplitude of obliquely incident p-polarized light when the magnetization $\mathbf{M}$, oriented perpendicular to the incidence plane, is reversed. In the structure of Fig. 1, this quantity is defined as [18]

$$\mathrm{TMOKE} = 2\frac{T_p(+\mathbf{M}) - T_p(-\mathbf{M})}{T_p(+\mathbf{M}) + T_p(-\mathbf{M})}, \tag{1}$$

where $T_p(\pm\mathbf{M})$ denotes the transmittance for $\mathbf{M}$ pointing along the $\pm\hat{\mathbf{e}}_z$ direction, respectively. Calculations of the transmittance, TMOKE and near fields were made using the

*william.carvalho@dtel.inatel.br
†jrmejia@inatel.br

 ©2021 American Physical Society

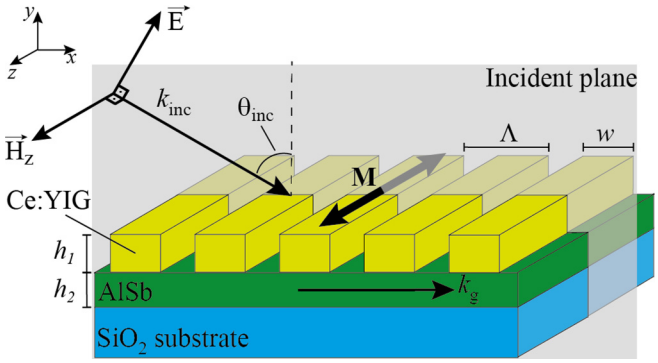

FIG. 1. Schematics of an all-dielectric system employed to enhance TMOKE. A Ce:YIG grating is deposited over an AlSb thin film, held by a SiO_2 substrate.

finite-element method (FEM) within the commercial software COMSOL MULTIPHYSICS. Floquet periodic boundary conditions were used along the x axis with perfect matched layers (PML) along the y boundaries. Numerical data were obtained for wavelengths (λ) in the range from 600 to 1000 nm, and the incident angle (θ_{inc}) from -20° to 60°. Numerical sweeps, with refined mesh sizes, were performed with steps of 0.05 nm and 0.005° for the wavelength and the incident angle, respectively.

The MO grating is considered as a periodic arrangement (along the x axis) of subwavelength rectangular wires of Ce:YIG placed along the z axis, as depicted in Fig. 1. The width and height of the ribs are denoted by w and h_1, respectively. A slab of AlSb III-V semiconductor with thickness h_2 is placed below the grating on a SiO_2 substrate. The corresponding real and imaginary components for the diagonal and off-diagonal components of the permittivity tensor are presented in Fig. 2 for all materials considered here. The anisotropic permittivity tensor ε_{MO} for the Ce:YIG ribs is written as [31]

$$\varepsilon_{\text{MO}} = \begin{pmatrix} \varepsilon_{xx} & i\varepsilon_{xy}m & 0 \\ -i\varepsilon_{yx}m & \varepsilon_{yy} & 0 \\ 0 & 0 & \varepsilon_{zz} \end{pmatrix}, \tag{2}$$

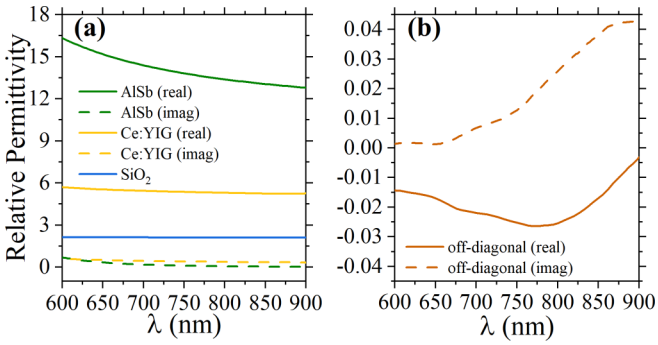

FIG. 2. Relative complex permittivity of the materials employed in the proposed systems. Diagonal components of the permittivity tensor are presented for (a) AlSb (gray color), Ce:YIG (red color), and SiO_2 substrate (blue). The real and imaginary off-diagonal components for the anisotropic Ce:YIG are presented in (b). Solid lines refer to the real part while the dashed lines correspond to the imaginary part.

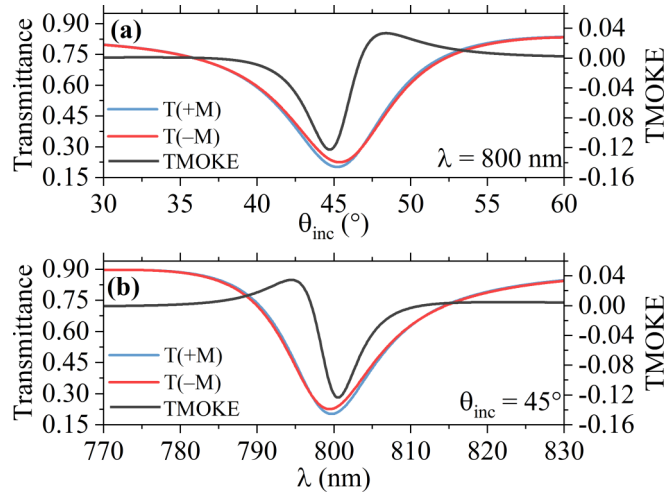

FIG. 3. Transmittances $T(+M)$, $T(-M)$, and TMOKE curves for (a) $\lambda = 800$ nm as a function of θ_{inc} and (b) $\theta_{\text{inc}} = 45^\circ$ as a function of λ. A strong Kerr effect of -12.33% was found in both cases.

where $\varepsilon_{xx} = \varepsilon_{yy} = \varepsilon_{zz}$ and $\varepsilon_{xy} = \varepsilon_{yx}$ are the complex diagonal and off-diagonal values of the permittivity tensor. $m = +1$ ($m = -1$) is used to indicate that the magnetization is pointing along the positive (negative) z axis. The diagonal components ε_{ii} ($i = x, y, z$) take their values from Figure 2(a) for Ce:YIG, whereas $\varepsilon_{xy} = \varepsilon_{yx}$ were taken [28,31] from Fig. 2(b). The isotropic permittivity for the HRI AlSb [33] ($\varepsilon_{\text{AlSb}}$) and SiO_2 [34] ($\varepsilon_{\text{SiO}_2}$) is obtained from Fig. 2(a). The choice of Ce:YIG is due to its compatibility with III-V and Si-based semiconductors [28–30], enabling straightforward integrability for on-chip MO applications.

III. RESULTS AND DISCUSSION

Let us first discuss the TMOKE enhancement from a subwavelength grating using a period length $\Lambda = 270$ nm, $w = 160$ nm, $h_1 = 120$ nm, and $h_2 = 110$ nm. The transmittance and TMOKE amplitudes are presented in Figs. 3(a) and 3(b) as functions of the incident angle and wavelength, respectively. Due to the high transparency of the materials in the grating nanostructure, the minima in the transmittance spectra in Fig. 3 are explained by the confinement and guiding of the electromagnetic field at the AlSb HRI slab. The incident electromagnetic field becomes resonantly coupled to the guided modes in the AlSb slab through the phase-matching condition [22]

$$k_{\text{inc}} \sin(\theta_{\text{inc}}) + p\frac{2\pi}{\Lambda} = k_{g,m}, \tag{3}$$

with k_{inc} and $k_{g,m}$ indicating the wave vectors for the incident and guided modes, respectively. Subindices g and m are used to indicate that the guided modes not only depend on the periodicity of the grating (g) but also on the magnetization sense along the z axis (m). p is an integer number that denotes the diffraction order. In contrast to recent approaches for TMOKE enhancement with grating structures, where the ribs and the slab on which they are placed were made of the same MO

material [22], our structure cannot be approached as a single effective layer. In order to highlight this conceptual difference, we calculated the dispersion equation for p-polarized modes as

$$\tan(d_2q_2) = \frac{\beta_2\beta_3(\beta_1+\beta_4)+\beta_2\left(\beta_3^2+\beta_1\beta_4\right)\tan(d_3q_3)}{\beta_3\left(\beta_2^2+\beta_1\beta_4+\beta_1\gamma_2-\beta_4\gamma_2-\gamma_2^2\right)+\left(-\beta_1\beta_3^2-\beta_2^2\beta_4+\beta_3^2\gamma_2-\beta_1\beta_4\gamma_2+\beta_4\gamma_2^2\right)\tan(d_3q_3)}, \tag{4}$$

where $\beta_i = \eta_{i,jj}q_i$, $q_i = \sqrt{\frac{\omega^2}{c^2}\frac{1}{\eta_{i,jj}} - k_x^2}$, $\gamma_2 = -\frac{im\varepsilon_{xy}}{\varepsilon_{jj}-\varepsilon_{xy}^2}k_x$, and

$$\eta_{i,jj} = \begin{cases} \frac{1}{\varepsilon_{i,jj}}, & i = 1,3,4, \\ \frac{\varepsilon_{i,jj}}{\varepsilon_{i,jj}^2-\varepsilon_{xy}^2}, & i = 2, \end{cases} \tag{5}$$

with subindex i indicating the corresponding medium ($i = 1$ for air; $i = 2$ for the effective MO slab; $i = 3$ for the AlSb slab; $i = 4$ for the SiO_2 substrate) and $j = x, y, z$. Calculations were made for a periodic arrangement of MO ribs as an effective medium slab. For the grating structure, k_x is related to $k_{g,m}$ through Eq. (3), which indicates that the TMOKE enhancement comes from the control of the phase matching between diffracted waves at the grating and guided modes in the HRI slab, in analogy to previous plasmonic mechanisms [18].

TMOKE amplitudes up to 12% are seen in Fig. 3, which are higher than in previous plasmonic approaches [18] using the waveguide-plasmon-polariton counterpart [26]. This TMOKE enhancement may be attributed to the different values for $k_{g,+M}$ and $k_{g,-M}$ [35], as it can be noted from the different $\lambda_{\pm M}$ and $\theta_{\pm M}$ for the transmittance minima. Transmittance and TMOKE spectra are shown in Figs. 4(a) and 4(b), respectively, for the same geometrical parameters in Fig. 3 but simultaneously varying λ and θ. It is noted that TMOKE can only be resonantly enhanced through the excitation of waveguide modes, i.e., where the transmittance becomes a minimum. The quality factor Q, defined as the ratio between the central resonance and the full width at half maximum (FWHM), was calculated for the results in Fig. 3 for $m = +1$. Using $Q_\lambda = \lambda_{res}/\Delta\lambda$ and $Q_\theta = \theta_{res}/\Delta\theta$, we obtained $Q_\lambda = 65.5$ and $Q_\theta = 6.21$. Since high Q factors indicate narrow bands, the approach may be useful for high-resolution sensing, for instance.

Upon varying the geometrical parameters for the grating in Fig. 1 systematically, we found another subwavelength

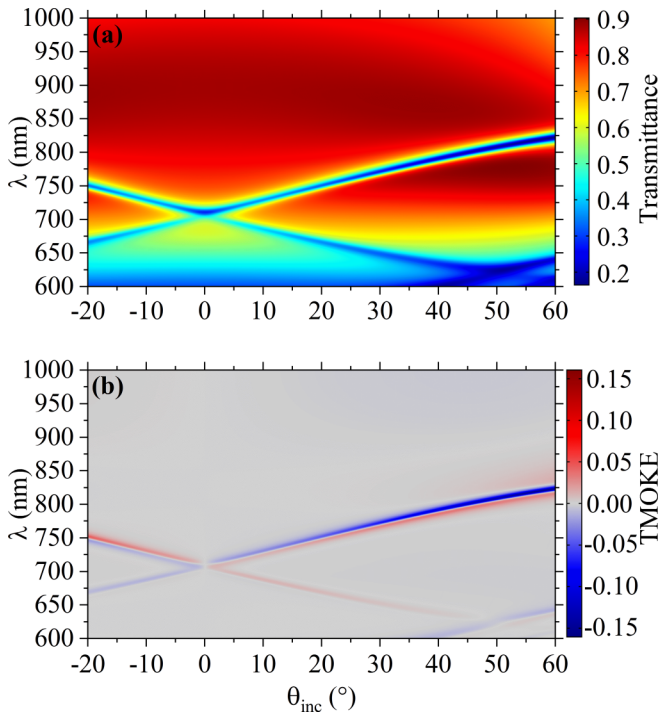

FIG. 4. Surface plot of (a) transmittance T and (b) TMOKE. A large T is observed for $\lambda > 750$ nm up to an incident wave angle of 60°.

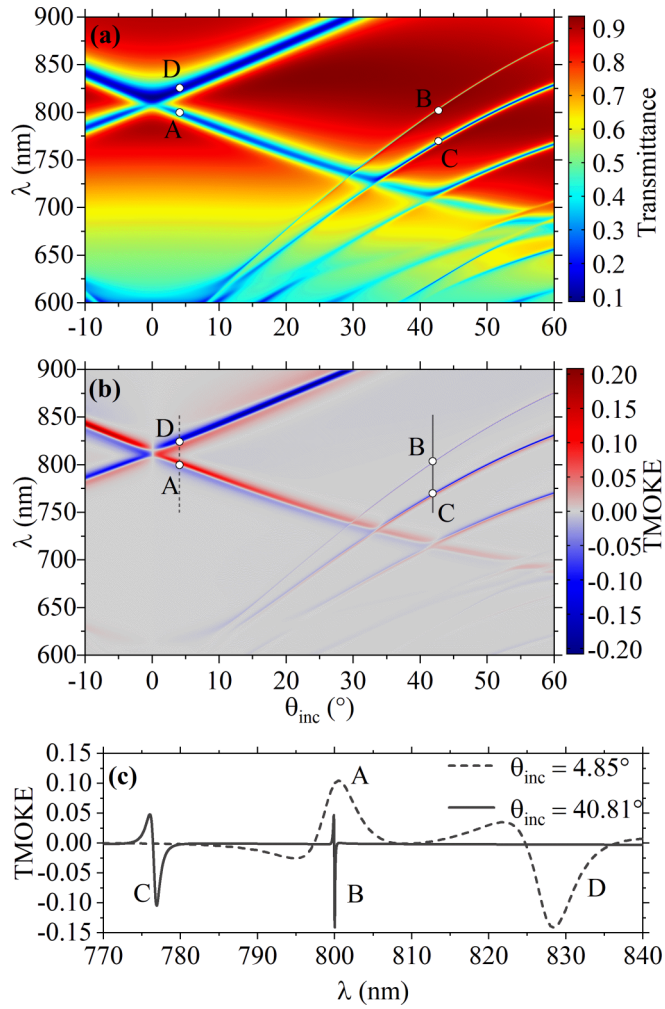

FIG. 5. Surface plot of (a) transmittance T, (b) TMOKE, and (c) TMOKE as a function of λ in two specific incident angles θ_{inc}.

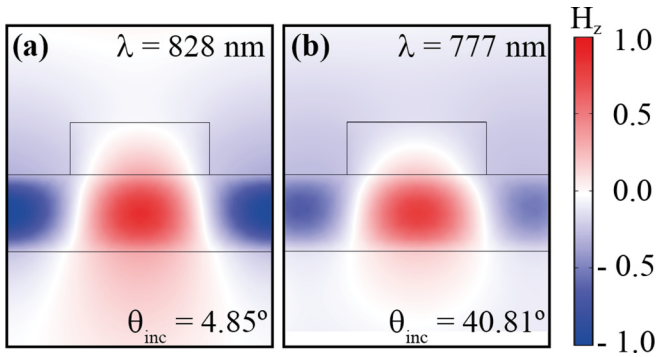

FIG. 6. Magnetic field profiles, Re(H_z), for the structures in (a) point D and (b) point C from Fig. 5.

geometry suitable for waveguiding at the HRI AlSb slab, with $\Lambda = 380$ nm, $w = 200$ nm, $h_1 = 75$ nm, and $h_2 = 110$ nm. It is significant that Ce:YIG films with this width and with the ribs can be developed by techniques such as pulsed laser deposition [28]. Several resonances for wide, narrow, or multiple peak TMOKE enhancements are observed for this structure in Figs. 5(a) and 5(b), where the transmittance and TMOKE spectra are shown as functions of the incident angle and wavelength. This set of resonances is caused by higher diffraction orders at smaller wavelengths, for which different FWHM and different Q factors are observed. In Fig. 5(c) we show the TMOKE spectra for fixed incident angles $\theta_{\text{inc}} = 4.85^\circ$ and $\theta_{\text{inc}} = 40.81^\circ$, denoted by dashed and solid lines. TMOKE resonances in this figure are labeled as A, B, C, and D, according to Fig. 5(b). The highest Q factors were obtained as $Q_{\text{B},\lambda} = 6267.59$ and $Q_{\text{C},\lambda} = 347.43$ for the TMOKE peaks labeled as B and C, indicating very narrow peaks and thus enabling high-resolution sensing.

The resonant coupling mechanism discussed here can be seen from Fig. 6, where the corresponding near fields for two different resonances from Fig. 5 are shown. Results were calculated (for $m = +1$) for $\lambda = 828$ nm ($\theta = 4.85^\circ$) and $\lambda = 777$ nm ($\theta = 40.81^\circ$). The TMOKE enhancement is reached by distributing the localized electromagnetic fields at the HRI slab inside the adjacent MO ribs, thus increasing their MO activity.

Although these results are promising for various applications, care must be taken with fabrication errors due to high Q factors. Results for the structure associated with point B in Fig. 5 are compared in Figs. 7(a)–7(d) with the cases where the parameters Λ, w, h_1, and h_2 suffer inaccuracies of the order of $\pm 5\%$. Special attention should be given to the lattice period Λ [see Fig. 7(a)] and the HRI slab thickness [see Fig. 7(d)], which strongly affect the phase-matching condition and waveguide resonances, respectively, while the rib width and height slightly affect the corresponding TMOKE amplitudes.

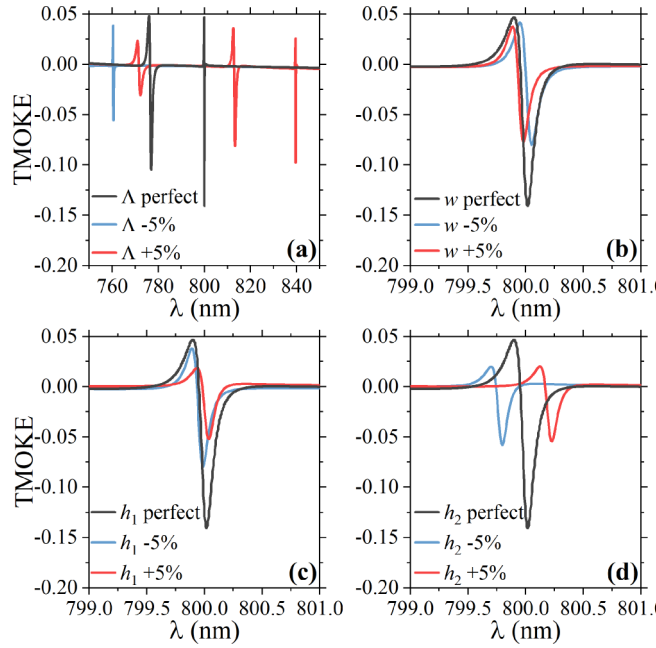

FIG. 7. Comparative results for the TMOKE associated with point B in Fig. 5, labeled perfect, with the structures having ± 5 % errors in their (a) period lengths (Λ), (b) rib widths (w), (b) rib heights (h_1), and (d) waveguide thickness (h_2).

IV. CONCLUSIONS

In conclusion, we have shown theoretically that MO dielectric gratings placed on a HRI slab can be used to produce enhanced TMOKE amplitudes. By changing the magnetization sense along the MO ribs we alter the resonant angle/wavelength, thus producing higher TMOKE amplitudes than in their magnetoplasmonic counterparts. Importantly, our proposal not only exhibits higher TMOKE amplitudes than magnetoplasmonic proposals but it also improves the efficiency through the use of low-loss dielectric materials. Furthermore, with the high Q factors observed, one may envisage potential applications in high-resolution sensing.

ACKNOWLEDGMENTS

We acknowledge the financial support from the Brazilian agencies FAPESP (2018/22214-6), the National Council for Scientific and Technological Development-CNPq (429496/2018-4, 305958/2018-6), and Coordination for the Improvement of Higher Education Personnel-CAPES (88882.365057/2019-01). Partial financial support was also received from RNP, with resources from MCTIC, Grant No. 01250.075413/2018-04, under the Radiocommunication Reference Center (Centro de Referência em Radiocomunicações - CRR) project of the National Institute of Telecommunications (Instituto Nacional de Telecomunicações - Inatel), Brazil.

[1] S. A. Dyakov, I. M. Fradkin, N. A. Gippius, L. Klompmaker, F. Spitzer, E. Yalcin, I. A. Akimov, M. Bayer, D. A. Yavsin, S. I. Pavlov, A. B. Pevtsov, S. Y. Verbin, and S. G. Tikhodeev, Phys. Rev. B **100**, 214411 (2019).

[2] O. V. Borovkova, H. Hashim, M. A. Kozhaev, S. A. Dagesyan, A. Chakravarty, M. Levy, and V. I. Belotelov, Appl. Phys. Lett. **112**, 063101 (2018).
[3] Q. Gui, Y. Zhou, S. Liao, Y. He, Y. Tanga, and Y. Wang, Soft Matter **15**, 393 (2019).
[4] E. Oblak, P. Riego, A. Garcia-Manso, A. Martínez-de-Guerenu, F. Arizti, I. Artetxe, and A. Berger, J. Phys. D: Appl. Phys. **53**, 205001 (2020).
[5] B. F. Diaz-Valencia, J. R. Mejía-Salazar, O. N. Oliveira, Jr., N. Porras-Montenegro, and P. Albella, ACS Omega **2**, 7682 (2017).
[6] K. J. Chau, S. E. Irvine, and A. Y. Elezzabi, IEEE J. Quantum Electron. **40**, 571 (2004).
[7] K.-S. Ho, S.-J. Im, J.-S. Pae, C.-S. Ri, Y.-H. Han, and J. Herrmann, Sci. Rep. **8**, 10584 (2018).
[8] D. Huang, P. Pintus, C. Zhang, P. Morton, Y. Shoji, T. Mizumoto, and J. E. Bowers, Optica **4**, 23 (2017).
[9] L. Luo, T. Tang, J. Shen, and C. Li, J. Magn. Magn. Mater. **491**, 165524 (2019).
[10] M. G. Manera, G. Pellegrini, P. Lupo, V. Bello, C. J. Fernández, F. Casoli, S. Rella, C. Malitesta, F. Albertini, G. Mattei, and R. Rella, Sens. Actuators, B **239**, 100 (2017).
[11] Š. Višňovský, E. Lišková-Jakubisová, I. Harward, and Z. Celinski, Opt. Mater. Express **7**, 2368 (2017).
[12] J. A. Girón-Sedas, F. Reyes Gómez, P. Albella, J. R. Mejía-Salazar, and O. N. Oliveira, Jr., Phys. Rev. B **96**, 075415 (2017).
[13] C. Rizal, Magnetochemistry **4**, 35 (2018).
[14] E. Moncada-Villa, O. N. Oliveira, Jr., and J. R. Mejía-Salazar, J. Phys. Chem. C **123**, 3790 (2019).
[15] V. I. Belotelov, I. A. Akimov, M. Pohl, V. A. Kotov, S. Kasture, A. S. Vengurlekar, A. V. Gopal, D. R. Yakovlev, A. K. Zevezdin, and M. Bayer, Nat. Nanotechnol. **6**, 370 (2011).
[16] G. Armelles, A. Cebollada, A. García-Martín, and M. U. Gonzáles, Adv. Opt. Mater. **1**, 10 (2013).
[17] M. Kataja, T. K. Hakala, A. Julku, M. J. Huttunen, S. van Dijkenm, and P. Törmä, Nat. Commun. **6**, 7072 (2015).
[18] L. E. Kreilkamp, V. I. Belotelov, J. Y. Chin, S. Neutzner, D. Dregely, T. Wehlus, I. A. Akimov, M. Bayer, B. Stritzker, and H. Giessen, Phys. Rev. X **3**, 041019 (2013).
[19] E. Gamet, B. Varghese, I. Verrier, and F. Royer, J. Phys. D: Appl. Phys. **50**, 495105 (2017).
[20] M. G. Barsukova, A. I. Musorin, A. S. Shorokhov, and A. A. Fedyanin, APL Photonics **4**, 016102 (2019).
[21] F. Royer, B. Varghese, E. Gamet, S. Neveu, Y. Jourlin, and D. Jamon, ACS Omega **5**, 2886 (2020).
[22] A. A. Voronov, D. Karki, D. O. Ignatyeva, M. A. Kozhaev, M. Levy, and V. I. Belotelov, Opt. Express **20**, 17988 (2020).
[23] S. S. Wang, R. Magnusson, and J. S. Bagby, M. G. Moharam, J. Opt. Soc. Am. A **7**, 1470 (1990).
[24] Y. Ding and R. Magnusson, Opt. Express **12**, 5661 (2004).
[25] Y. H. Ko and R. Magnusson, Optica **5**, 289 (2018).
[26] A. Christ, S. G. Tikhodeev, N. A. Gippius, J. Kuhl, and H. Giessen, Phys. Rev. Lett. **91**, 183901 (2003).
[27] V. G. Kravets, A. V. Kabashin, W. L. Barnes, and A. N. Grigorenko, Chem. Rev. **118**, 5912 (2018).
[28] M. C. Onbasli, L. Beran, M. Zahradník, M. Kučera, R. Antoš, J. Mistrík, G. F. Dionne, M. Veis, and C. A. Ross, Sci. Rep. **6**, 23640 (2016).
[29] L. Bi, J. Hu, P. Jiang, H. S. Kim, D. H. Kim, M. C. Onbasli, G. F. Dionne, and C. A. Ross, Materials **6**, 5094 (2013).
[30] M. C. Onbasli, T. Goto, X. Sun, N. Huynh, and C. A. Ross, Opt. Express **22**, 25183 (2014).
[31] E. Moncada-Villa and J. R. Mejía-Salazar, Sensors **20**, 952 (2020).
[32] S. Sadeghi and S. M. Hamidi, J. Magn. Magn. Mater. **493**, 165709 (2020).
[33] A. B. Djurišić, E. H. Li, D. Rakić, and M. L. Majewski, Appl. Phys. A **70**, 29 (2000).
[34] I. H. Malitson, J. Opt. Soc. Am. **55**, 1205 (1965).
[35] A. E. Khramova, D. O. Ignatyeva, M. A. Kozhaev, S. A. Dagesyan, V. N. Berzhansky, A. N. Shaposhnikov, S. V. Tomilin, and V. I. Belotelov, Opt. Express **27**, 33170 (2019).